JATIS Journal of Astronomical Telescopes, Instruments, and Systems

RESEARCH PAPER

Extreme broadband dichroics: Monte Carlo transmission line modeling for astronomical spectroscopy

Vinooja Thurairethinam,[a,*] **Giorgio Savini**,[a] **Gary Hawkins**,[b] **and Paolo Chioetto**[c]

[a]University College London, Department of Physics and Astronomy, London, United Kingdom
[b]University of Oxford, Infrared Multilayer Laboratory, Oxford, United Kingdom
[c]Institute for Photonics and Nanotechnologies (IFN), National Council of Research of Italy (CNR), Padova, Italy

ABSTRACT. Dichroic beamsplitters, or dichroics, rely on the optical interference that occurs within thin-film layers to ensure the separation of the transmission and reflection of selective wavelengths of an incident beam of light at a given angle of incidence. Utilized within the optical systems of numerous space telescopes, they act to separate the incoming light spectrally and spatially into various channels. As space missions increasingly demand simultaneous observations across wavebands spanning extreme wavelength ranges, the necessity for exceedingly complex broadband dichroics has emerged. Subsequently, the uncertainties pertaining to their optical performance have also become more intricate. We use transmission line modeling to evaluate the spectral performance of multilayer coatings deposited on a substrate material for given thicknesses, materials, angles of incidence, and polarization. A dichroic recipe in line with the typical specifications and requirements of a dichroic is designed with the aid of a Monte Carlo simulation. The tolerances of the coating performance to systematic and random uncertainties from the manufacturing process, as well as from environmental changes in space, are studied. With the aid of accurate manufacturing recipes and uncertainty amplitudes from commercial manufacturers, this tool can predict variations in the optical performance that result from the propagation of each of these uncertainties for various hypothetical scenarios and systematic effects.

 [DOI: 10.1117/1.JATIS.10.1.018005]

Keywords: space telescopes; dichroic filters; dichroic performance; optical coatings; Monte Carlo simulation; systematics

Paper 23138G received Nov. 16, 2023; revised Feb. 8, 2024; accepted Feb. 28, 2024; published Mar. 15, 2024.

1 Introduction

Astronomical spectroscopy requires precise filtering to reject undesirable spectral radiation while maximizing the throughput within the required isolated passband.[1,2] Dichroic beamsplitters, or dichroics, are filters that rely on the optical interference occurring within thin-film layers to ensure the transmission and reflection of selective wavelengths from an incident light beam. They play a vital role in determining spectral response measurements and are, thus, critical optical components for selecting and isolating wavebands for astronomical observation.[3] The performance of the coating ensures that the precise spectral requirements of the dichroics are upheld, including the high spectral position accuracy and environmental durability, while optimizing the

*Address all correspondence to Vinooja Thurairethinam, vinooja.thurairethinam.20@ucl.ac.uk

2329-4124/2024/$28.00

performance of the filter. The design and manufacture of such a multilayer system requires careful consideration of various parameters to ensure that the spectral requirements are satisfied. The selection of coating materials is essential in determining the transmission and reflection wavebands as well as the flatness of the responses across these wavelength regions.

Several space telescopes have used these optical components to divide incident light into several spectral components for a myriad of scientific instruments. The James Webb Space Telescope (JWST) uses dichroic beamsplitters for both the Near-Infrared Camera (NIRCam) and the Mid-Infrared Instrument (MIRI). NIRCam consists of two optical modules, both of which are further divided into two channels using a dichroic filter, providing a total of four channels for NIRCAM. This enables simultaneous observations in both short- ($0.6\ \mu\text{m} \leq \lambda \leq 2.3\ \mu\text{m}$) and long-wavelength ($2.4\ \mu\text{m} \leq \lambda \leq 5.0\ \mu\text{m}$) bands.[4,5] Similarly, MIRI also consists of four channels separated by sets of three dichroic filters. These four channels are further split into three wavelength ranges using a separate set of three dichroics for each of the three wavelength ranges. Here, the most broadband of these dichroics is the dichroic 1-c, which has a reflection band of $6.45\ \mu\text{m} \leq \lambda \leq 7.77\ \mu\text{m}$ and a transmission band of $9.87\ \mu\text{m} \leq \lambda \leq 28.83\ \mu\text{m}$.[6]

Additionally, the dichroic filter of the Euclid space telescope acts to separate visible and near-infrared light for the two instruments on the spacecraft, the visible imager (VIS) and the near-infrared spectrometer and photometer (NISP). The substrate is coated on the incident side with a dichroic multilayer coating and an anti-reflection coating on its rear surface to improve the performance in its transmissive waveband, thus reflecting wavelengths of $550\ \text{nm} \leq \lambda \leq 900\ \text{nm}$ toward VIS and transmitting wavelengths of $920\ \text{nm} \leq \lambda \leq 2000\ \text{nm}$ toward NISP.[7]

Moving beyond visible and infrared light, the application of dichroics stretches across a wide range of other wavelengths. The Galaxy Evolution Explorer (GALEX), which operates within the ultraviolet, uses a dichroic system to project images simultaneously onto two different detectors. The dichroic is designed to reflect light of wavelength $1350\ \text{Å} \leq \lambda \leq 1750\ \text{Å}$ and transmit wavelengths of $1750\ \text{Å} \leq \lambda \leq 2800\ \text{Å}$. In this way, the instrument can perform high-resolution imaging, as well as spectroscopy, in the two wavebands.[8,9]

Transitioning from past and ongoing missions, on the horizon, the Atmospheric Remote-sensing Infrared Exoplanet Large-survey (Ariel) telescope is a fourth medium-class mission in ESA's Cosmic Vision program with the objective of performing spectroscopic observations of a large population of known exoplanets, anticipated to launch in 2029.[10] Its waveband of 0.5 to 7.8 μm is separated spatially and spectrally into the numerous channels of its instruments by a system of several dichroic beamsplitters and some mirrors, including the extreme broadband dichroic, D1, as portrayed in Fig. 1. The primary purpose of D1 is the spectral division of the

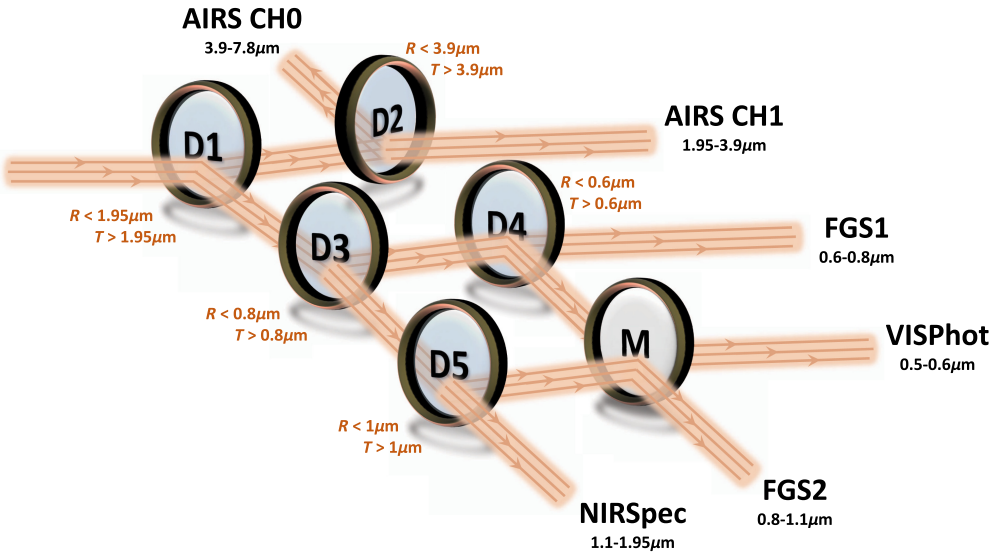

Fig. 1 A simplified schematic of the Ariel optical configuration showing the light path from the telescope optical system to the detectors of the FGS and AIRS modules. This portrays the concept of using a dichroic and mirror system to separate light spatially and spectrally into various channels.

Table 1 Ratios of the maximum and minimum wavelengths of the spectral bands of various instruments.

Instrument	Ratio of reflection band	Ratio of transmission band
JWST NIRCam	3.83	2.08
JWST MIRI	1.20	2.92
Euclid	1.64	2.17
GALEX	1.33	1.67
Ariel	3.90	4.00

incident beam of the telescope into two wavebands corresponding to the two instrument modules, FGS and AIRS, which requires the reflection of wavelengths of 0.5 μm $\leq \lambda \leq$ 1.95 μm and the transmission of wavelengths of 1.95 μm $\leq \lambda \leq$ 7.8 μm.

One way to quantify the broadness of the bandwidths of this dichroic is the ratio of the maximum and minimum wavelengths of the pass and stop bands, with a higher ratio indicating a more broadband dichroic. The results of these ratios are shown in Table 1. In the case of Ariel, these spectral bandwidth ratios for the reflection and transmission regions equate to 3.90 and 4.00, respectively, which are both well beyond any of the previously mentioned examples.

2 Methodology

The transmission line model presented in this article allows for the simulation of the performance of a multilayer system, as well as the impacts of uncertainties on this performance. To obtain an optimized multilayer design in line with the performance requirements of the component, a Monte Carlo (MC) simulation is conducted. The sensitivity of the acquired design is then studied in a tolerance analysis to predict the worst offenders to its performance.

2.1 Modeling Optical Multilayer Coatings

Multilayer systems can be modeled using the formalism outlined in Ref. 11 in which each layer is assumed to be homogeneous, smooth, and parallel-facing. The D1 dichroic is comprised of N thin-film layers of specified materials and thicknesses deposited on both of its surfaces. The performance of the front coating on which the light is incident and the rear anti-reflection coating, which prevents ghost imaging, were modeled individually, bounded by two semi-infinite media – a lossless vacuum and the substrate. In the case of linearly polarized light, the Fresnel reflection $\rho_{i,i+1}$ and transmission coefficients $\tau_{i,i+1}$ at the interface between layers i and $i+1$, for an angle of incidence, θ, is given as

$$\begin{aligned}
\text{p-polarised:}\ \rho_{i,i+1} &= \frac{n_i \cos(\theta_{i+1}) - n_{i+1} \cos(\theta_i)}{n_i \cos(\theta_{i+1}) + n_{i+1} \cos(\theta_i)}, \quad \tau_{i,i+1} = \frac{2n_i \cos(\theta_i)}{n_i \cos(\theta_{i+1}) + n_{i+1} \cos(\theta_i)} \\
\text{s-polarised:}\ \rho_{i,i+1} &= \frac{n_i \cos(\theta_i) - n_{i+1} \cos(\theta_{i+1})}{n_i \cos(\theta_i) + n_{i+1} \cos(\theta_{i+1})}, \quad \tau_{i,i+1} = \frac{2n_i \cos(\theta_i)}{n_i \cos(\theta_i) + n_{i+1} \cos(\theta_{i+1})},
\end{aligned} \tag{1}$$

where n_i is the refractive index of the i'th layer and θ_i is the angle of the light incident to this layer.

The dispersion and temperature dependence of the medium were integrated into the model through the use of wavelength and temperature-dependent expressions for the refractive index. Moreover, dielectric losses due to absorption were accounted for using a complex refractive index $n_{c,i}$ in the form of

$$n_{c,i} = n_{r,i}(\lambda, t) - jk_i(\lambda, t), \tag{2}$$

where $n_{r,i}$ is the real refractive index and k_i is the extinction coefficient. Both the real refractive index and the extinction coefficient can be wavelength- and temperature-dependent, where λ is

the wavelength of light and t is the temperature of the material. This provides a comprehensive description of the material, encompassing the refractive as well as the absorption properties.

We define a propagation and matching matrix. The propagation matrix is used to propagate electric fields through a single layer i – from one interface to the coating and to the following interface. This is defined as

$$P_i = \begin{bmatrix} \exp(j\phi_i) & 0 \\ 0 & \exp(-j\phi_i) \end{bmatrix}, \tag{3}$$

where j is the imaginary unit and ϕ_i is the phase thickness of layer i. The phase thickness of a coating is given as

$$\phi_i = \frac{2\pi}{\lambda} n_{c,i} d_i \cos(\theta_i), \tag{4}$$

where d_i is the physical thickness of layer i.

Then, the behavior of the electric fields traveling from one side of an interface to the other side of the interface is represented using a matching matrix of the form

$$M_{i,i+1} = \frac{1}{\tau_{i,i+1}} \begin{bmatrix} 1 & \rho_{i,i+1} \\ \rho_{i,i+1} & 1 \end{bmatrix}. \tag{5}$$

The matrices of Eqs. (3) and (5) are multiplied in succession to obtain the resulting transfer matrix S. In this framework, S describes the relation between the incident field amplitude E_1^+, reflected field amplitude E_1^-, and transmitted field amplitude E_{N+1}^+ as follows:

$$\begin{bmatrix} E_1^+ \\ E_1^- \end{bmatrix} = S \begin{bmatrix} E_{N+1}^+ \\ 0 \end{bmatrix}, \tag{6}$$

where we assume that there are no backward waves in the exit medium. The introduced transfer matrix S takes the form of

$$S = \begin{bmatrix} s_1 & s_2 \\ s_3 & s_4 \end{bmatrix}, \tag{7}$$

and is calculated using

$$S = M_{0,1} P_1 M_{1,2} P_2 \ldots P_N M_{N,N+1}. \tag{8}$$

Assuming an incident field amplitude of 1, the reflectance R and transmittance T are inferred using

$$R = \left| \frac{s_2}{s_1} \right|^2 \quad T = \frac{n_{c,N+1}}{n_{c,0}} \left| \frac{1}{s_1} \right|^2, \tag{9}$$

where $n_{c,0}$ and $n_{c,N+1}$ are the complex refractive indices of the incident and exit media, respectively.

Subsequently, the primary reflection of the entire component is assumed to be that of the front coating. The transmissions of the two sets of coatings are combined with the absorption due to the substrate to obtain the overall transmission profile of the dichroic by calculating the product of these efficiencies. This additional absorption term takes into consideration the attenuation of the light intensity as it propagates through the substrate, which is expected to be the dominant absorption component of the dichroic in the case of D1. This is a direct result of the thickness of the substrate of 1 cm surpassing the cumulative thickness of the coatings of D1 by a factor of around 1000. This was explicitly found using

$$I = I_0 \exp\left[-\alpha_s \frac{d_s}{\cos(\theta_{r,s})} \right], \tag{10}$$

where d_s is the physical thickness, $\theta_{r,s}$ is the refractive angle of the beam within the substrate, and α_s is the absorption coefficient of the substrate. The absorption coefficient has a direct relation to the complex refractive index of the material in the form of

$$\alpha = \frac{4\pi k}{\lambda}, \tag{11}$$

where k is the extinction coefficient.

2.1.1 *Design and optimization of spectral performance*

In principle, this model may be adapted and used as a tool to study any given optical multilayer coating component. This paper showcases the application of this tool to our design of a dichroic conforming to the requirements of the complex broadband dichroic of the Ariel mission, D1. At the time of writing, D1 was in its developmental stages, and the recipe of the actual D1 dichroic and its materials were not made available to the authors by the industrial manufacturers. Although an accurate manufacturing recipe would be ideal, with a design of similar spectral performance, the results displayed in this paper are also representative of the dichroic and thus can be used to estimate its expected performance.

The dichroic presented in this paper was designed to consist of a ZnSe substrate coated on the incident side with over fifty layers of alternating coating layers of ZnSe ($n_H \sim 2.6$) and YbF3 ($n_L \sim 1.5$) as the high refractive index (H) and low index (L) layer, respectively. A broadband anti-reflection (BBAR) coating covers the rear surface of the substrate to minimize ghosting reflections, which also consist of alternating layers of ZnSe and YbF3. The dispersion and absorption behavior of ZnSe and YbF_3 were implemented using models of complex refractive indices adopted from Ref. 12. Additionally, various types of beams can be defined to be incident on the dichroic. For this particular scenario, a collimated beam from the telescope arrives at the dichroic at an angle of incidence of 12 deg, so all calculations were done under the assumption of a constant angle of 12 deg. This light was considered to be unpolarized, so the two spectra obtained from the p-polarized and s-polarized cases were averaged. However, it is possible to simulate various polarization states separately.

An MC simulation was then executed to randomly create slight variations in the thicknesses of a few randomly selected layers, with the goal of acquiring a set of thicknesses that will fulfill the spectral requirements of the component. In the case of D1, this target function equates to a maximum reflection at $0.5 \leq \lambda \leq 1.95$ μm and a maximum transmission at $1.95 \leq \lambda \leq 7.8$ μm. The transition wavelength, defined to be the wavelength at which the transmission is 50%, is designed to be 1.95 μm. Initially, the initial maximum step size is set to 20% of the thicknesses. The sum of squared residuals between each prior spectrum and the spectral performance are obtained after each MC iteration for 14,000 equally-spaced wavelength points along the complete waveband. This provides a quantifying parameter to evaluate the scale of improvement in the randomly altered recipe of thicknesses. The thickness of each of the coating layers is constrained to values between 10 and 450 nm to address potential physical limitations of the deposition machine and coating durability. If an improvement that meets both the thickness and performance specifications was acquired, the altered recipe was temporarily accepted and taken to be an updated reference design for the following MC iteration. Conversely, if the produced design did not yield an improved spectral performance, the reference design remained unchanged, and the step size was reduced by half. The thicknesses were continuously altered in this manner until a suitable performance with minimal interference fringes within the region of interest was acquired. The final thicknesses obtained thus generate a spectral design in agreement with the requirements of the multilayer component and are taken to be the final recipe of the coating.

Similar refinement methods are frequently used to adjust the parameters, such as the thicknesses of coating layers, of a starting design until a satisfactory performance is achieved.[13] However, constraints on the thicknesses of layers must also be considered. Thicker layers are often subject to mechanical failure in the form of fractures during thermal cycling testing and may reduce spectral throughput through increased absorption, in comparison with thinner layers.[14] Hence, an initial set of estimated thicknesses of each layer was selected to provide a reasonable approximation to the required performance, with the thicknesses of the layers being limited to a maximum of 450 nm. Moreover, the number of layers should be limited to the minimum required to obtain the desired performance. An excessive number of coating layers may

lead to complications during the manufacturing and compliance testing processes of the component, for example, due to fracturing from internal stress or delamination (see, e.g., Ref. 15).

The authors acknowledge that more efficient design software is available. However, to maintain complete control over the underlying physics influencing the performance of the dichroic, an ab initio approach was used. The design and optimization of the dichroic is not the primary focus of the study but rather a means to obtain a design that could facilitate a study of the diverse systematics and their subsequent physical implications on the coating performance while maintaining control over the physics involved in the output.

2.2 Sources of Uncertainty

Discrepancies between the predicted and measured performance of an optical component composed of a multilayer coating can be attributed to a number of uncertainties. This paper explores some of the most significant sources of uncertainty and their impact on the performance of the component. The deviation of the spectral performance from the nominal performance as a result of each scenario was found to examine the wavelengths that are most sensitive to these manufacturing uncertainties, as well as the potential discrepancies in the spectral performance.

2.2.1 *Manufacturing uncertainties*

The thin-film layers of the coating are deposited onto the substrate in sequence. Accurate control of the thicknesses of the individual layers, as well as adequate knowledge of the refractive indices of the materials, are both required for the manufacture of a multilayer coating.[16] However, minor irreproducible variations during the manufacture can occur outside the parameter controls of the deposition process. These unpredictable errors were simulated as 10,000 random fluctuations in the form of a Gaussian distribution with a standard deviation dictated by the accuracy of the instrument and technique used for this procedure. The value of this uncertainty should be confirmed with the manufacturers of the dichroic. For the case of D1, the uncertainty was approximated from the Bühler IBS 1600 tool, which is able to deposit coatings with a uniformity of $\pm 0.5\%$.[17]

In addition to random fluctuations, systematic errors within the thicknesses can stem from inaccurate termination during the deposition process of the layer.[18] This may be a direct result of insufficient sensitivity to the final thickness during the deposition of the layer or the failure to identify a fluctuation or systematic variations in the deposition conditions.[19] These complications, in turn, relate to the accuracy of the equipment used for the deposition process, which we assumed to be 0.5% once again.

Furthermore, coating layers frequently have optical properties that differ slightly from their bulk counterparts due to the different columnar microstructures in thin films, which is dependent on the deposition conditions.[16,20,21] For the work described here, a scenario of a systematic error of -0.1% was considered for the index of YbF_3.

2.2.2 *Environmental changes in space*

The operation of a dichroic at cryogenic temperatures introduces further uncertainties. The Ariel telescope system is passively cooled to cryogenic temperatures of ~50 K for its required sensitivity and stability.[22] The effect on the spectral performance of the multilayer structure of thermal fluctuations of the environment during operation must be considered. In the case of Ariel, temperature fluctuations of approximately ± 0.5 K are expected to occur during the course of an observation.[23] The indices of refraction of ZnSe and YbF_3 at the required cryogenic temperatures have not been published in any literature currently known to the authors.

The effect of temperature on the performance of the dichroic was modeled using the temperature-dependent Sellmeier constants of ZnSe provided by Ref. 24, verified for temperatures of $93.2\ \text{K} \leq T \leq 473.2\ \text{K}$. This model was subsequently linearly extrapolated to 50 K as this value does not reach far outside the verified temperature range. Additionally, the refractive index of ZnSe notably appears to have a relatively weak temperature dependence, with minor changes in $n(\lambda)$ between 93.2 and 473.2 K, as can be seen in Fig. 2. Thus, a linear extrapolation of the model to lower cryogenic temperatures is a reasonable approximation. This model of the

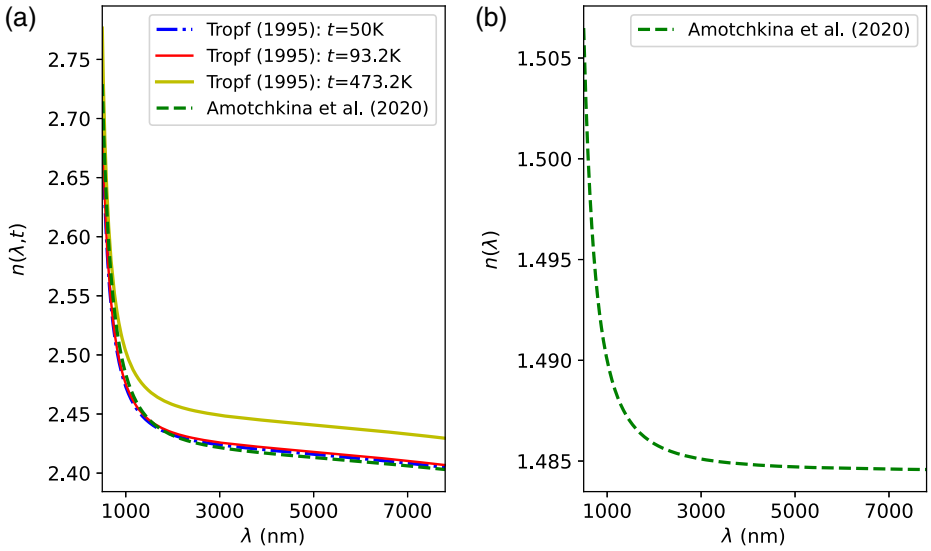

Fig. 2 Temperature-dependent models of the refractive indices of the chosen materials as a function of the Ariel waveband. (a) and (b) The materials ZnSe and YbF_3, respectively. (a) The solid lines represent values calculated directly from each model within the temperature and wavebands for which the model was confirmed, adopted from Ref. 24. The blue dashed line in (a) indicates extrapolated values of the model to a temperature of 50K. The dashed green lines in both plots show the model adopted from Ref. 12, which assumes no temperature dependence.

refractive index of ZnSe from Ref. 24 was used to obtain an alternative nominal performance, only to be used in the study of the effects of temperature fluctuations on the spectral performance as this refractive index model lacks absorption information for Znse. To address this limitation, for the remaining scenarios studied, we refer to the ZnSe model from Ref. 12, to retain the absorption behavior of the ZnSe coating layers and substrate. The discrepancy between the nominal performances of the dichroic using the two models of the ZnSe refractive index is insignificant as a result of the minor difference between the wavelength-dependent refractive indices from Refs. 24 and 12, as shown in Fig. 2. On the other hand, the temperature-dependent refractive index of YbF_3 is not available in the literature, so no temperature dependence was included for this material.

This paper also studies the scenario of a collimated beam slightly shifted with respect to the expected angle of incidence, to take into consideration the beam being unlikely to align perfectly with the angle of incidence requirement. We explore an example of a -0.1 deg shift with respect to the D1 dichroic angle of incidence of 12 deg.

In addition, molecular contamination can also degrade the performance of optical components in a space environment, resulting in an optical throughput loss due to changes in the reflection and transmission and increased absorption. We evaluate the predicted performance and assess the magnitude of the spectral effect of contaminant films deposited on the exterior surfaces of a dichroic. The optical performance of the contaminated dichroic is modeled as before, now with additional layers of contamination on the front and rear surfaces of the component. The contamination is assumed to have taken the form of a thin-film layer with a homogenous thickness across the surface of the component.

The potential primary contaminants on space telescopes include water ice and a number of non-volatile residuals (nvr), which are currently unidentified. Consequently, in addition to water ice, tetramethyl-tetraphenyl trisiloxane (DC-704) was included in the model as a silicone contaminant analog, the photochemical deposition of which has been commonly studied.[25–27] DC-704 has been shown to deposit as a smooth, widely-spread film on nonmetallic, cold surfaces for temperatures up to 93K due to inadequate thermal energy to induce the coalescence of molecules.[28] Moreover, in a recent study conducted for JWST, DC-704 was identified to be one of the primary potential contaminants, with its origin attributed to silicone fluids used in diffusion pumps for high vacuum systems.[29]

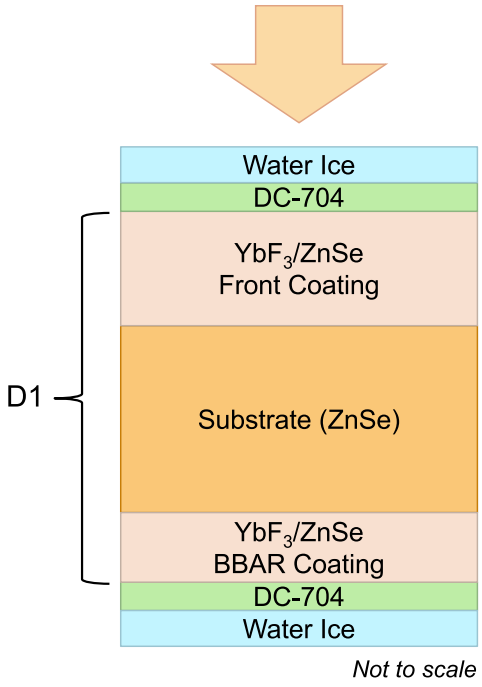

Fig. 3 A schematic representation of the multilayer contamination model. The front and rear coatings of the Ariel D1 dichroic, consisting of alternating layers of YbF_3 and ZnSe deposited on a ZnSe substrate, are assumed to be coated on both sides with a layer of DC-704 and water ice. The depositions are assumed to be ideal, with all layers being smooth and parallel-facing. The arrow shows the direction of the incident light.

The contaminant assumed to deposit onto the surface first is expected to be the nvr, DC-704. The contaminant remains in a gaseous, vapor-like state following the vacuum pumping process and begins to deposit onto optical surfaces during the cooling process. In due course, the water ice is expected to form on the optical surfaces. The multilayer structure is shown in Fig. 3. The refractive index of DC-704 is modeled as a constant value from Ref. 30. The dispersion and absorption information of this material are not presently included as this was not available to the authors at the time of writing. The water ice is modeled using the refractive index found by Ref. 31, in which the optical constants of ice are provided from ultraviolet to microwave wavelengths.

3 Results and Discussion

3.1 Modeling Optical Multilayer Coatings

A design of a dichroic in agreement with the Ariel dichroic D1 specifications with the optimization of its performance in accordance with its specifications using an MC simulation was performed. With this, the recipe of the dichroic was optimized using an MC simulation to yield the closest acceptable approximation to the desired spectral performance in line with the requirements of D1.

Figure 4 shows the spectral profile of the optimized D1-like design for an angle of incidence of 12 deg obtained from the MC simulation. The recipe consists of alternating layers of $YbF3_3$ and ZnSe, with a front coating of 55 layers and a rear BBAR coating of 11 coating layers. The MC simulation optimizes the thickness of each layer to be a unique non-quarter-wave fractional thickness to reduce the ripple amplitude within the spectrum. The simulated spectrum of the dichroic shows high reflectance in the FGS waveband and high transmittance within the AIRS channels. Despite the presence of interference fringes within the FGS channels, the design nonetheless exceeds the minimum reflection and transmission requirements at all wavelengths. These interference fringes are characteristic of the visible and near-infrared waveband due to changes in phase shift experienced by the light. The phase change, which is dependent on the

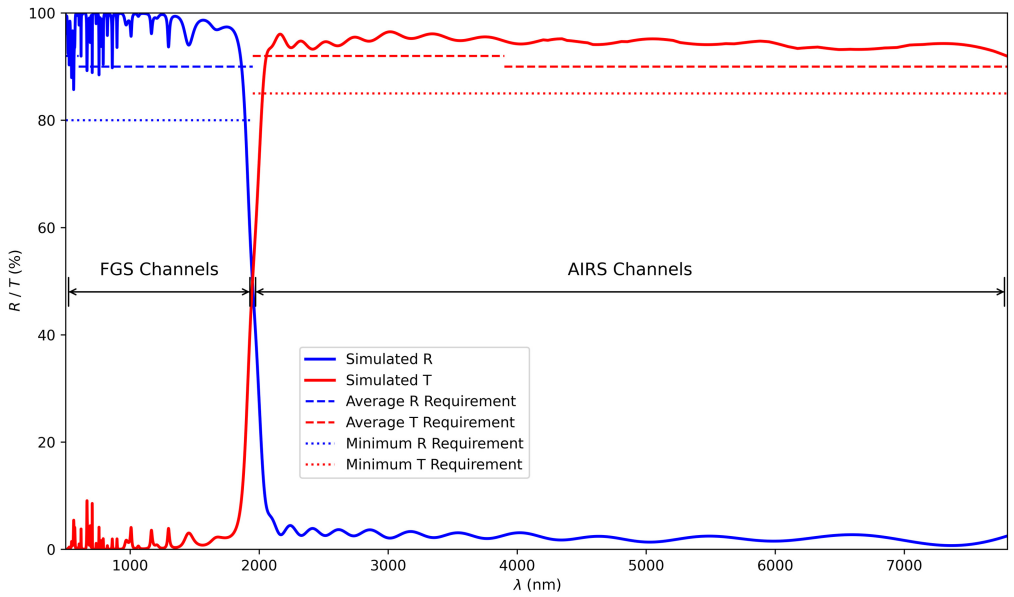

Fig. 4 Spectral profile of the dichroic design with a front and rear coatings at an angle of incidence of 12 deg. The simulated transmission and reflection are plotted as solid red and blue lines, respectively. The respective dashed lines indicate the average required performance of D1 for a given waveband, and the dotted lines represent the minimum performance requirements.

Table 2 Performance parameters of designed dichroic and performance requirements.

	Average R (%)		Average T (%)	
Wavelengths (nm)	$500 < \lambda < 600$	$600 < \lambda < 1750$	$1950 < \lambda < 3900$	$3900 < \lambda < 7800$
Required	92.0	90.0	92.0	90.0
Designed	96.4	98.3	93.8	94.1

refractive index of the medium and the thickness of the coating layer, changes as a result of the refractive index steeply decreasing with the wavelength. Consequently, the phase shift induced by a given layer is more substantial at the lower wavelengths, so the interference effects are more pronounced. The MC simulation aims for the optimal overall spectral performance and will, therefore, not be able to compensate for significant variations in the refractive index of the materials at lower wavelengths.

Moreover, the performance in reflection surpasses the average reflection requirements of 92% for $500 < \lambda < 600$ nm and 90% for $600 < \lambda < 1750$ nm, with an average reflection of 96.4% and 98.3%, respectively. Similarly to the reflectance, the transmittance surpasses the average requirements of 92% for $1950 < \lambda < 3900$ nm with an average transmittance of 93.8%, and 90% for $3900 < \lambda < 7800$ nm with 94.1% (Table 2). The simulated transmittance of this design shows a smooth spectral response for the AIRS channels, with the magnitude of the interference fringes within the FGS waveband reduced by the addition of a BBAR coating. The transition from the stopband to the passband also closely matches the requirement of 1950 nm with a transition wavelength in reflectance of 1950.0 nm and in transmittance of 1948.6 nm at the boundary between the FGS and AIRS channels by design.

3.2 Sources of Uncertainty

Several sources of uncertainty were modeled to illustrate their influence on the nominal performance of the dichroic and its multilayer coating to assess the worst offenders to the performance. Figure 5 depicts a contoured 2D histogram of the changes in performance resulting from 10,000 randomly generated errors within ±0.5% on the thicknesses of the coating layers. These random

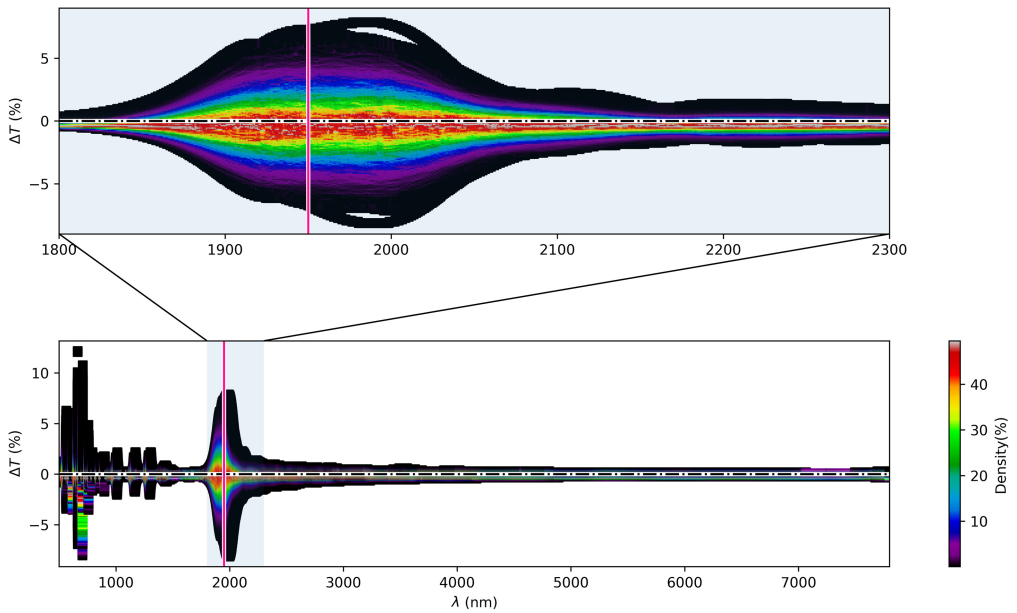

Fig. 5 Contoured 2D histogram of the posterior distribution of the spectral deviations from 10,000 random ±0.5% thickness errors on the coating layers. The deviations at each wavelength are binned into bins of width $\Delta T = 0.1\%$, with the density percentage of the total 10,000 generated errors of each bin indicated by the color bar. A dashed black line marks $\Delta T = 0$, and a solid pink line shows the nominal transition wavelength.

errors in the thicknesses of the coating layers may result from the limited intrinsic precision of the deposition process, such as the consistency of optical monitoring to correctly terminate the deposition of a thin film. Each altered recipe of thicknesses generates a spectrum with a deviation in the nominal performance, with 10,000 such variations for each wavelength point. The distribution of these deviations shown in Fig. 5 reveals a smooth vertical color bar gradient centered near the $\Delta T = 0$ axis at all wavelengths. This indicates a Gaussian distribution of deviations centered around the nominal transmission of the dichroic, suggesting a stable build with the performance of the dichroic remaining close to its design despite the presence of random deposition errors. The enlarged portion of the contoured 2D histogram reveals that the centers of the distributions were shifted narrowly beneath the $\Delta T = 0$ line at higher wavelengths, which is expected. The optimization process aims to increase transmission in this region. Thus any errors or deviations from this optimized recipe will most likely yield a deterioration in performance and, hence, a decreased overall transmission. The deviations within the passband, where transmission is designed to be high, remain modest due to the high performance of the coating in this waveband.

Some noticeable performance changes are visible within the high-reflectance region, with higher deviations occurring at the wavelengths at which the ripples are present in Fig. 4. Due to the sensitivity of the interference behavior of the coating to coating thicknesses, any small fluctuations in the recipe can lead to changes in the spectral response of the dichroic. This results in changes in the combinations of destructive and constructive interference, particularly as the wavelengths at which the ripples are already present. However, the most prominent variations from the nominal transmission coincide with the transition wavelength region. As opposed to the areas of maximum transmission and reflection, where the primary objectives of a design are optical efficiency and an improvement in performance, the focus in the region of the transition is its exact location within the waveband. The deviation in the transmission of up to ±8.1% in this region reveals the propensity of the transition wavelength to be shifted. Such a shift toward a lower wavelength than the nominal transition wavelength implies an increased transmission, whereas a displacement to a higher wavelength results in a decreased transmission at the nominal transition wavelength. Both of these cases seem equally likely, as shown by the vertical symmetry of this feature in Fig. 5. These random errors can be used in simulating the random variations in the coating layer thicknesses across the coating surfaces for a single deposition of the layers. Consequently, this may result in deviations in the phase of the light across a coating

Table 3 Maximum deviation of nominal transmission due to each of the different types of sources of uncertainty near the transition wavelength region.

Source of uncertainty	Maximum $\lvert\Delta T\rvert$ (%)
Random d_i errors ($\leq \pm 0.5\%$)	8.134
Systematic d_i redundancy (+0.5%)	5.661
Systematic d_i deficiency (−0.5%)	5.689
Uncertainty in n_L (−0.1%)	0.225
Shift of θ (−0.1 deg)	0.033
Systematic T increase (+0.5 K)	0.009
Systematic T decrease (−0.5 K)	0.009

surface, which has been observed for the dichroic of the Euclid mission.[32] However, this is beyond the scope of this paper and will be addressed in future work.

Alongside random coating thickness errors, a systematic coating layer thickness error in the form of a consistent deficiency or surplus of 0.5% in all layers of the dichroic coating was also modeled. Figure 6 shows the resulting deviation near the transition wavelength of up to $\Delta T = +5.69\%$ at 1908.5 nm in the case of the deficiency and $\Delta T = -5.66\%$ at 1917.5 nm for the surplus. The considerable number of coating layers, which includes some relatively large thicknesses, leads to an increased design sensitivity to systematic thickness errors. This induces a shift in the positions of the transition to lower and higher wavelengths for the cases of deficiency and surplus, respectively. Thus, more significant systematic errors are likely to cause an increase in the shift of this transition wavelength. The changes in transmission are most substantial at the lower wavelength ranges, where the interference fringes are seen. The MC process defines the thicknesses to be optimized to reduce the ripple amplitude in this region. Therefore, any change in the thicknesses causes this design to be less than optimal. This leads to an undesirable increase in the ripple amplitude. The maximum deviation for a systematic thickness deficiency occurs at $\lambda = 706.0$ nm, with a variation of $\Delta T = -8.23\%$. The maximum variation from the nominal performance for the systematic thickness surplus is $\Delta T = +8.55\%$ at $\lambda = 709.5$ nm. Similarly to the case for systematic deposition errors, the changes in transmission near the transition wavelength remain inconsequential, with levels of $\Delta T < 0.3\%$ for all of the remaining scenarios. In the case of a refractive index error, as a result of uncertainty in the knowledge of the YbF_3 index values, the most considerable deviation from the nominal transmission around the transition region of $\Delta T = 0.23\%$ occurs at 2006.0 nm (Table 3). A consistent variation in the index of YbF_3 causes the refractive index of over half of the coating layers to be changed slightly. Consequently, the phase shift experienced by the light as it passes through these layers is changed, which affects the interference conditions as well as the degree of interferences at different wavelengths.

In comparison with the deviations in the nominal performance due to manufacturing uncertainties, the changes due to potential environmental changes during the operation of the dichroic in space tend to be much lower in amplitude. The expected difference in performance due to temperature fluctuations throughout an Ariel observation is negligible, with a maximum variation around the transition region of $\Delta T = \pm 0.009\%$ at 2826.0 nm, where the spectral variation of an increase and decrease in the temperature remains symmetric about the $\Delta T = 0$ axis. A variation in transmittance is visible in the mid-infrared region of Fig. 6(a), which is solely due to the difference in refractive index models used for ZnSe. The cryogenic performance of the component is affected due to the effects of temperature on the optical constants of the materials, so the physical effects are similar to a refractive index uncertainty in ZnSe, but of very low amplitude. Moreover, the effect of a collimated incident beam that arrives at 11.9 deg, rather than 12 deg, has an insignificant impact on the spectral performance of the dichroic, with a maximum variation around the transition region of 0.03% at 1850.5 nm. The interference conditions within the dichroic coating are affected by the angle of incidence of the light. A modification in the angle

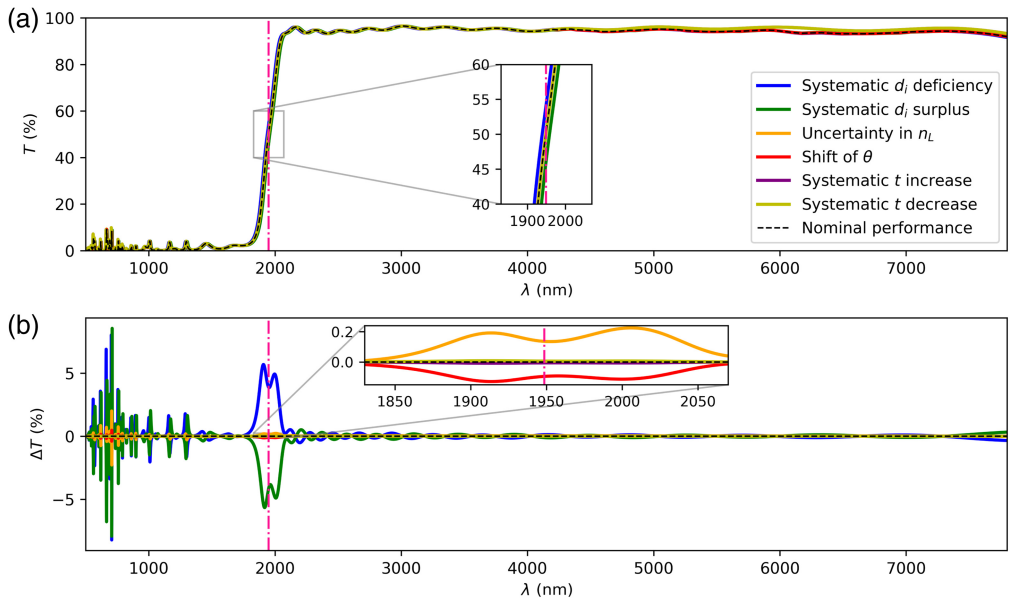

Fig. 6 Change in the nominal transmission of the dichroic due to a range of systematic effects of the D1-like design. (a) and (b) The transmission spectra resulting from the change in the parameters and the change in transmission from the nominal transmission, respectively. In both plots, the nominal performance is shown by a dashed black line, and the vertical dotted-dashed line marks the transition wavelength of the nominal performance. The blue and green lines indicate the case of a −0.5% and +0.5% systematic thickness error, respectively, in all coating layers. The orange line shows the scenario of a decrease of 0.1% in the refractive index of YbF_3 due to uncertainty in the knowledge of the refractive index. The result of a beam shifted by −0.1 deg from the requirement of an angle of incidence of 12 deg is shown in red. Finally, the purple and yellow lines indicate the case of a temperature offset as an increase and decrease of 0.5 K, respectively, with the performance at 50K taken to be the nominal transmission.

of incidence can, therefore, cause a change in the magnitude of constructive and destructive interference at various wavelengths. Figure 6 establishes that small changes in beam angles are unlikely to have a significant effect on the performance of the dichroic.

3.2.1 *Synergistic effects of sources of uncertainty*

Two or more of the sources of uncertainty explored within this paper can be combined to explore their synergistic effects on the performance of the dichroic. Figure 7 shows the changes in performance as a result of a systematic deposition error of $+0.5\%$ and -0.5% in all layers, combined with 10,000 randomly generated errors within $\pm 0.5\%$ on the thicknesses of the coating layers. This delves into the possibility of a manufactured dichroic recipe differing from the intended design due to the intrinsic precision of the deposition machine, along with an inconsistency within the termination of the depositions. Similarly to Fig. 5, this result shows a smooth vertical color bar gradient, indicating a Gaussian distribution of the deviations of the performance of the dichroic. However, unlike the case of random deposition errors alone, this combination of effects leads to the center of the color bar gradient being shifted. Comparing Figs. 7 to 6, one can see that the center is shifted from $\Delta T = 0$ to being at the deviation in transmission ΔT caused by a systematic thickness error alone. Both cases of a systematic thickness error of $+0.5\%$ and -0.5% shown in Figs. 7(a) and 7(b), respectively, follow this pattern. This is expected as the systematic deposition error initially changes the performance of the dichroic, so all consequent uncertainties applied from the model will be applied to this amended performance.

3.2.2 *Transition wavelength shifts*

To further investigate these shifts in transition wavelength observed for the different systematic effects, the correlation of these shifts with each source of uncertainty was studied. A line was

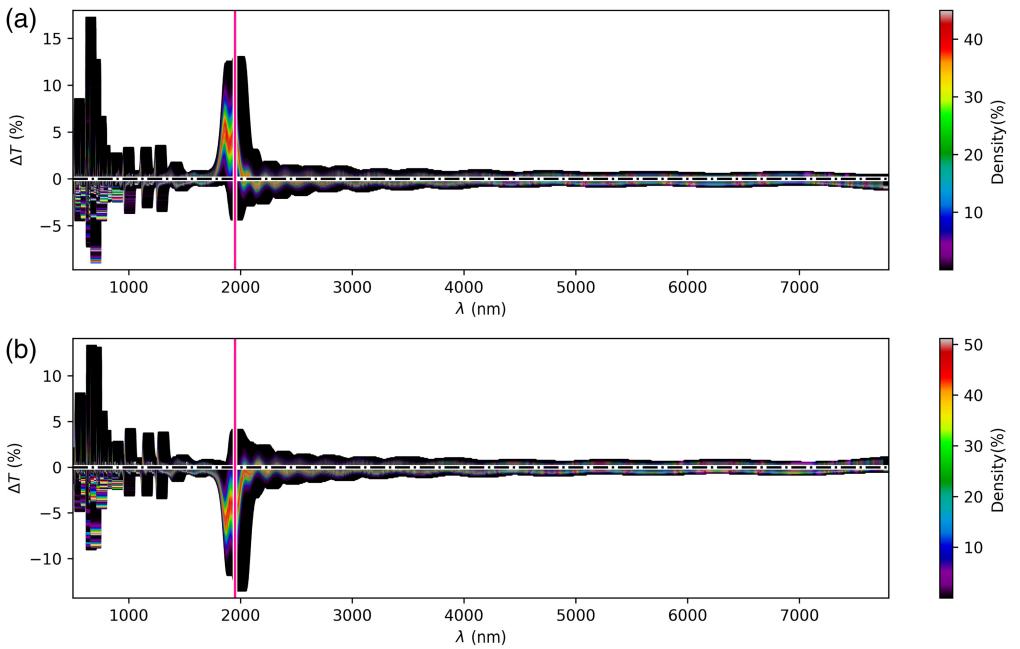

Fig. 7 Contoured 2D histogram showing deviation from nominal transmission due to random ±0.5% thickness errors and a systematic thickness error of ±0.5%. (a) and (b) The cases of the same set of 10,000 random errors within ±0.5% thickness errors applied to a systematic thickness error of +0.5% and −0.5%, respectively. The deviations at each wavelength are binned into bins of width $\Delta T = 0.1\%$, with the density percentage of the total 10,000 generated errors of each bin indicated by the color bar. A dashed black line marks $\Delta T = 0$, and a solid pink line shows the nominal transition wavelength.

fitted to the slope of the transition section of the spectrum shown in Fig. 4. This slope and its gradient, m, are used to predict the shift in the transition wavelength using

$$m = \frac{\Delta T}{\Delta \lambda}, \tag{12}$$

where ΔT is the change in transmission observed at the nominal transition wavelength and $\Delta\lambda$ is the shift in the transition wavelength.

Therefore

$$\Delta \lambda = \frac{T_{\text{unc}} - 50\%}{m}, \tag{13}$$

where T_{unc} is the transmission at the nominal transition wavelength of the spectrum resulting from a given source of uncertainty. This shift in transition wavelength is calculated directly using Eq. (13) for all scenarios of various systematic effects.

The results of this investigation are shown in Fig. 8, with the gradient of the transition for the D1-like dichroic found to be 0.41 nm^{-1}. The shift in transition wavelength correlates linearly with each source of uncertainty. Coating layer thickness errors, uncertainty in the refractive index, and offsets in temperature show a positive correlation, whereas a negative correlation is observed for the offsets in the angle of incidence. The transition wavelength shifts shown in Fig. 8 directly correspond to the amplitude of ΔT in Fig. 6. This can be most clearly seen in the case of systematic layer thickness errors, for which the shifts in the transition wavelength displayed in Fig. 8 range from −9.95 to +10.83 nm. For a systematic deposition deficiency of 0.5% on all coating layers, a transition wavelength shift of −8.30 nm was predicted, hence placing the new transition wavelength in transmission at 1940.3 nm. Comparing this with Fig. 6, this prediction agrees with the high change in transmission observed at this wavelength.

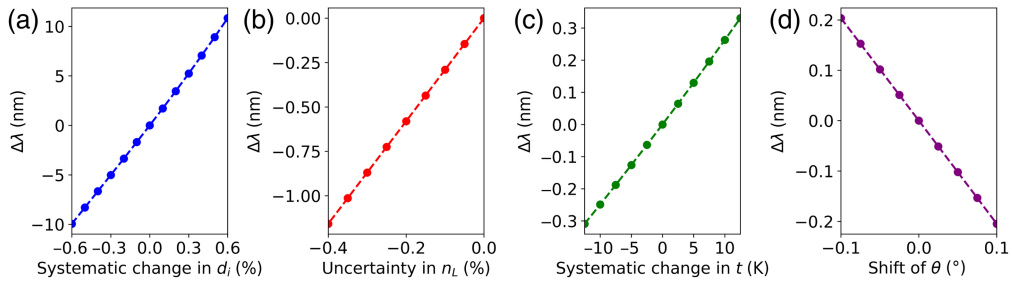

Fig. 8 Shift in transition wavelength in transmission due to each systematic effect. (a) and (b) The transition wavelength shifts found for a range of relative systematic coating thickness errors and relative uncertainties in the knowledge of the refractive index of YbF_3, respectively. (c) and (d) The scenarios of temperature offsets from the nominal average operating temperature of 50 K and a variation in the angle of incidence from the nominal angle of 12 deg.

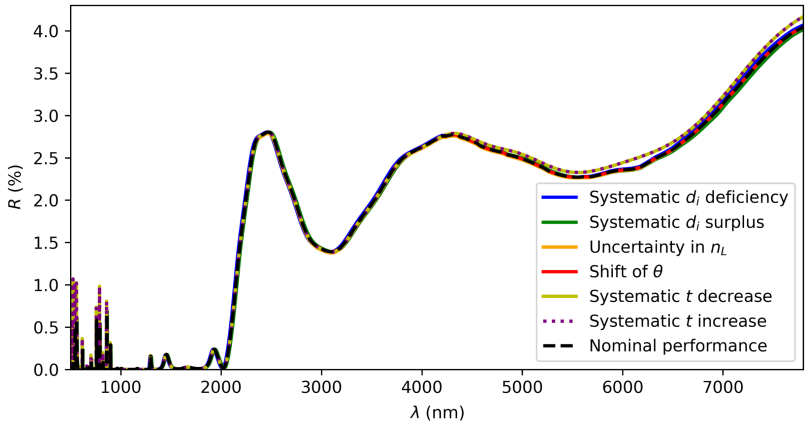

Fig. 9 Expected amplitude of ghosting reflections. The amplitude of ghosting reflections from the nominal simulated spectral profile of the dichroic is plotted as a dashed black line. The cases of the various systematic effects previously presented in this paper are also shown.

3.3 Ghosting Effects

A broadband AR coating covers the rear surface of the dichroic to minimize ghosting reflections and reduce unwanted reflections. Despite the primary reflection of the dichroic being assumed to be that of the front coating, the rear coating also produces a reflective component of the beam. However, given the large thickness of the substrate of 1cm, it is assumed that no coherent interference occurs between the two coatings, so the interference calculations of the two coatings are kept separate. The residual fraction of the beam that is reflected from the rear coating of the dichroic once again travels through the substrate and front coating to create a ghost beam, shifted with respect to the beam reflected from the front coating. The expected amplitude of these ghosts in the reflection for our D1-like dichroic is depicted in Fig. 9. In the case of the nominal optical performance, the effect of ghosts is more significant within the higher wavelength region but remains of low intensity. This is a foreseeable consequence of the design specifications of D1. Most of the light within the stopband will be reflected at the incident surface and will thus not reach the BBAR coating. On the other hand, light within the near- and mid-infrared is intended to be transmitted through the rear side of D1. Hence, any unwanted reflections from the rear side will be more pronounced at these wavelengths. The various systematics cause a minor shift in the nominal ghost amplitudes as a function of wavelength, but the changes remain comparable and relatively low.

3.4 Molecular Contamination and Water Ice

Molecular contamination can deposit onto optical surfaces and cause degradation of the performance of optical components in a space environment. The spectral response of the D1 dichroic as

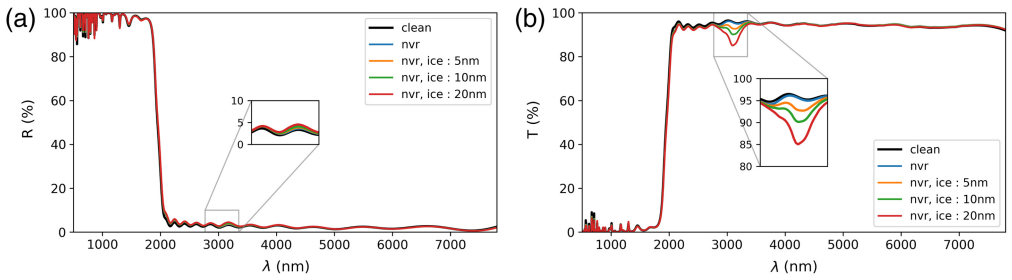

Fig. 10 Reflectance and transmittance spectra resulting from contamination deposited on the front and rear surfaces of the D1-like model, as portrayed in Fig. 3. The uncontaminated, clean sample is plotted in black. (a) and (b) The spectral performance of the contaminated model in reflectance and transmittance. The thickness of the DC-704 layers is assumed to be 20 nm for all contaminated models, and the thickness of the ice layers is varied.

a result of contamination being deposited on both surfaces of the dichroic, as illustrated in Fig. 3, is shown in Fig. 10. The most prominent effect of the contamination on the spectral performance is a direct result of the additional absorption that was introduced.

In reflection, the increased absorption results in larger interference fringes within the lower waveband of the reflective region. On the other hand, at 2000 to 3000 nm, the contamination slightly increases the reflectance. The layers of contamination contribute to the interference effects within the multilayer coating and thus cause interference effects at these wavelengths of light. This results in increased reflectance, with the magnitude of this effect being dependent on the thickness of the contaminant films. As the thickness of the water ice layer increases, the reflectance also increases. However, this occurs within the passband region, designed for high transmission, and is, therefore, an undesirable effect. The reflectance is modeled to be solely affected by the incident coating of the dichroic, whereas the transmittance is given by both coatings. Hence, the transmittance is affected by the contamination deposited on both sides of the dichroic, whereas the reflectance is merely affected by the contamination on the incident surface. This reduced interaction with the contaminants is likely to cause any absorption features to be less prominent in the reflectance of the dichroic. Moreover, multiple reflections within the multilayer coating may partially compensate for any absorption feature that may otherwise be present.

Conversely, the transmitted light interacts in a more pronounced manner with the cumulative effect of the absorption from the contaminants on the front and rear sides of the dichroic. The transmission does not benefit from partial compensation. The addition of DC-704 alone significantly reduces the overall transmittance within the majority of the passband wavelengths. The layer of nvr acts as an additional coating layer with a differing refractive index and slightly alters the performance. As the nvr itself has not been modeled to be absorptive, this effect can be attributed to further interference effects and a change in the effective optical path length, adversely affecting the transmission of the dichroic. Additionally, the feature centered on $\lambda = 3115$ nm is a result of the strong absorption band that is characteristic of water ice in the mid-infrared region.[33] This effect is correlated to the thickness of the water ice layers causing increased absorption, and therefore, the size of the absorption feature becomes more apparent.

4 Conclusion

Using this model, we were able to predict the tolerance of a dichroic beamsplitter to various levels of uncertainty that may affect its optical performance. This paper explored the application of this model to a dichroic design in compliance with the requirements of Ariel D1, which is considered to be a complex extreme broadband dichroic. A design in accordance with the spectral specifications of the dichroic was obtained with high reflectivity for a visible and near-infrared rejection stop-band, as well as a wide passband, offering transparency for wavelengths spanning the near-infrared to mid-infrared. Nonetheless, it is worth noting that the accuracy of this model is restricted by the accuracy of the parameter models provided. The optimization process to obtain a suitable recipe for coating thicknesses provides a set of very precise values. However, practically,

the deposition process has limited precision, so the recipe can only be produced to the limit of the precision of the deposition machine. This further justifies the study of the distribution of random and systematic thickness variations in this paper.

Deviations in performance were shown to be correlated with wavelengths at which interference fringes are present within the design and can thus be expected in those regions. In addition, various systematics may result in the shifting of the transition wavelength of the dichroic filter. Uncertainties in the thicknesses of the coating layers were shown to be the worst offenders to the performance of a dichroic and the designed position of the transition wavelength. On the other hand, temperature and angle of incidence offsets were likely only to have a minor effect on the expected performance. The uncertainties outlined here must be taken into consideration to achieve the desired performance of a dichroic beamsplitter.

Moreover, a potentially significant limitation of this model is the assumption that the coating layers are entirely uniform. Extreme broadband dichroics often consist of a considerable number of layers, which likely results in scattering due to the increased risk of non-uniformities at the interfaces of these layers, particularly for non-normal incidences. This model does not consider losses due to the surface roughness and the resultant scattering, which pertains to not only the optical coating layers but also any potential contamination. Contamination, by definition, is not uniform, which yields a roughness across the surface of the optical component, resulting in a randomized phase error across the surface. The reliability of the performance of these dichroic filters plays a crucial role in ensuring that the precise spectral requirements are upheld while increasing the performance sensitivity of an instrument.

Disclosures

The authors have no competing interests to declare.

Code and Data Availability

The code used in this study can be found on GitHub at https://github.com/vinthurai/ASTRALIS. The necessary files and data required to run the script are included in this repository.

Acknowledgments

The authors would like to acknowledge that parts of the methodology of this paper were previously submitted as an SPIE Proceedings paper for Astronomical Telescopes + Instrumentation 2022.[34] This work was funded by the Science and Technology Facilities Council (STFC), UK Research and Innovation (UKRI).

References

1. G. Hawkins and R. Hunneman, "A spectral performance model for the high resolution dynamics limb sounder (6 – 18 μm)," *Infrared Phys. Technol.* **41**(4), 239–246 (2000).
2. G. J. Hawkins et al., "Infrared filters and coatings for the high resolution dynamics limb sounder (6 – 18 μm)," *Appl. Opt.* **39**(28), 5221–5230 (2000).
3. G. Hawkins and R. Sherwood, "Cooled infrared filters and dichroics for the James Webb Space Telescope mid-infrared instrument," *Appl. Opt.* **47**(13), C25–C34 (2008).
4. S. D. Horner and M. J. Rieke, "The near-infrared camera (NIRCam) for the James Webb Space Telescope (JWST)," *Proc. SPIE* **5487**, 628–634 (2004).
5. J. P. Gardner et al., "The James Webb Space Telescope mission," *Publ. Astron. Soc. Pac.* **135**(1048), 068001 (2023).
6. M. Wells, G. Hawkins, and G. Olofsson, "The design and fabrication of multiple dichroic beamsplitters for the MIRI spectrometer (4.8-29 μm)," *Proc. SPIE* **5487**, 794–803 (2004).
7. L. M. G. Venancio et al., "Euclid payload module: telescope characteristics and technical challenges," *Proc. SPIE* **9143**, 91430I (2014).
8. O. H. Siegmund et al., "High-resolution cross delay line detectors for the Galex mission," *Proc. SPIE* **3765**, 429–440 (1999).
9. O. H. Siegmund et al., "The Galex mission and detectors," *Proc. SPIE* **5488**, 13–24 (2004).
10. G. Tinetti et al., "The science of ARIEL (Atmospheric Remote-Sensing Infrared Exoplanet Large-Survey)," *Proc. SPIE* **9904**, 99041X (2016).
11. H. A. Macleod, *Thin-Film Optical Filters*, Optical Science and Technology (2007).

12. T. Amotchkina et al., "Characterization of e-beam evaporated Ge, YbF_3, ZnS, and LaF_3 thin films for laser-oriented coatings," *Appl. Opt.* **59**(5), A40–A47 (2020).
13. J. Dobrowolski and R. Kemp, "Refinement of optical multilayer systems with different optimization procedures," *Appl. Opt.* **29**(19), 2876–2893 (1990).
14. G. Hawkins, R. Sherwood, and K. Djotni, "Mid-infrared filters for astronomical and remote sensing instrumentation," *Proc. SPIE* **7101**, 710114 (2008).
15. B. F. Sørensen et al., "Thermally induced delamination of multilayers," *Acta Material.* **46**(8), 2603–2615 (1998).
16. B. T. Sullivan and J. A. Dobrowolski, "Deposition of metal/dielectric multilayer filters," *Proc. SPIE* **2253**, 1213–1217 (1994).
17. A. Ribeaud et al., "Infra-red multi-layer coatings using YbF_3 and ZnS in an ion beam sputtering system," in *Opt. Interference Coat.*, Optical Society of America, p. MC–7 (2019).
18. H. H. Bauer and E. Nuessler, "In situ optical multichannel spectrometer system," *Proc. SPIE* **2253**, 423–431 (1994).
19. B. T. Sullivan and J. Dobrowolski, "Deposition error compensation for optical multilayer coatings. I. Theoretical description," *Appl. Opt.* **31**(19), 3821–3835 (1992).
20. A. Dirks and H. Leamy, "Columnar microstructure in vapor-deposited thin films," *Thin Solid Films* **47**(3), 219–233 (1977).
21. F. Flory et al., "Interpreting anisotropy and disturbances of optical properties of thin films in terms of layer microstructure," *Proc. SPIE* **2253**, 1232–1242 (1994).
22. G. Morgante et al., "Thermal architecture of the ESA ARIEL payload," *Proc. SPIE* **10698**, 106984H (2018).
23. G. Morgante et al., "The thermal architecture of the ESA ARIEL payload at the end of phase b1," *Exp. Astron.* **53**, 905–944 (2022).
24. W. J. Tropf, "Temperature-dependent refractive index models for BaF_2, CaF_2, MgF_2, SrF_2, LiF, NaF, KCL, ZnS, and ZnSe," *Opt. Eng.* **34**(5), 1369–1373 (1995).
25. P. A. Boeder et al., "Effect of a silicone contaminant film on the transmittance properties of AR-coated fused silica," *Proc. SPIE* **5526**, 32–43 (2004).
26. G. S. Arnold, R. C. Y. Owl, and D. F. Hall, "Optical effects of photochemically deposited contaminant films," *Proc. SPIE* **1329**, 255–265 (1990).
27. G. S. Arnold and K. T. Luey, "Photochemically deposited contaminant film effects," *Proc. SPIE* **2864**, 269–285 (1996).
28. K. T. Luey, K. R. Olson, and D. J. Coleman, "Optical system contamination: formation of films and droplets," *J. Astron. Telesc. Instrum. Syst.* **4**(3), 036001 (2018).
29. N. S. Abraham, "Application of molecular adsorber coatings in chamber a for the James Webb Space Telescope," in *Contamin., Coat., Mater., and Planet. Prot. (CCMPP) Workshop, (GSFC-E-DAA-TN44340)* (2017).
30. Gelest, "Material safety data sheet - safety data sheet sit7757.0," 2015, https://livchem-logistics.com/wp-content/uploads/2017/03/SIT7757.0-msds.pdf (accessed 22 July 2023).
31. S. G. Warren, "Optical constants of ice from the ultraviolet to the microwave," *Appl. Opt.* **23**(8), 1206–1225 (1984).
32. L. M. G. Venancio et al., "Coating induced phase shift and impact on euclid imaging performance," *Proc. SPIE* **9904**, 99040V (2016).
33. J. W. Schaaf and D. Williams, "Optical constants of ice in the infrared," *JOSA* **63**(6), 726–732 (1973).
34. V. Thurairethinam et al., "Monte Carlo transmission line modelling of multilayer optical coatings for performance sensitivity of a dichroic filter for the ARIEL Space Telescope," *Proc. SPIE* **12180**, 1218048 (2022).

Vinooja Thurairethinam is a PhD student in the astrophysics group at University College London (UCL). Her research focuses on optical modeling techniques for the dichroic filters used in the Ariel Space Mission (ESA). She is particularly interested in the effects of potential systematics on the spectral performance of these optical components, impacting the precision of the spectroscopic observations of the Ariel Mission.

Giorgio Savini obtained his master's degree in physics and his PhD in astronomy at the University of Rome "La Sapienza." He worked on the Planck satellite's HFI and the Herschel Space Observatory at Cardiff University (UK). Since 2009, he has been at UCL, and as of 2018, he holds the position of professor in astrophysics, specializing in infrared astrophysics and instrumentation. Currently, he serves as the payload scientist on the Ariel Space Mission (ESA) and UK Calibration convener for Litebird (JAXA). He has co-authored over 260 papers in physics and astronomy.

Gary Hawkins received his PhD from the University of Reading for research focusing on optical thin-film engineering. He is the group leader of the Infrared Multilayer Laboratory (IML) with more than 30 years of experience in the spectral design and manufacturing of advanced thermal infrared optical interference coatings used in planetary remote sensing and astronomical instruments. His research interests include the study, design, and manufacture of high-performance thin-film interference multilayers, optical materials, filters, and coatings.

Paolo Chioetto holds a PhD in sciences, technologies, and measurements for space from Padova University. He is a researcher at the Institute for Photonics and Nanotechnologies in Padova. His experience includes optical and opto-mechanical analysis and design, optical simulations, characterization and calibration of optical instruments, optical metrology, and characterization of optical coatings. Since 2018, he has been working for ESA's Ariel mission, where he currently serves as the AIV Manager for the telescope assembly.